





## Article

# Enhancing Mass Transport in Organic Redox Flow Batteries Through Electrode Obstacle Design

Joseba Martínez-López <sup>1</sup>, Unai Fernández-Gamiz <sup>1,\*</sup>, Eduardo Sánchez-Díez <sup>2</sup>, Aitor Beloki-Arondo <sup>3</sup> and Íñigo Ortega-Fernández <sup>3</sup>

<sup>1</sup> Nuclear Engineering and Fluid Mechanics Department, University of the Basque Country UPV/EHU, Nieves Cano 12, 01006 Vitoria-Gasteiz, Spain; joseba.martinezl@ehu.eus

<sup>2</sup> Centre for Cooperative Research on Alternative Energies (CIC EnergiGUNE), Basque Research and Technology Alliance (BRTA), Alava Technology Park, Albert Einstein 48, 01510 Vitoria-Gasteiz, Spain; esanchez@cicenergigune.com

<sup>3</sup> TECNALIA Research & Innovation, Basque Research and Technology Alliance (BRTA), Mikeletegi Pasealekua 2, 20009 Donostia-San Sebastian, Spain; aitor.beloki@tecnalia.com (A.B.-A.); inigo.ortega@tecnalia.com (Í.O.-F.)

\* Correspondence: unai.fernandez@ehu.eus

**Abstract:** This study examines the impact of incorporating obstacles in the electrode structure of an organic redox flow battery with a flow-through configuration. Two configurations were compared: a control case without obstacles (Case 1) and a modified design with obstacles to enhance mass transport and uniformity (Case 2). While Case 1 exhibited marginally higher discharge voltages (average difference of 0.18%) due to reduced hydraulic resistance and lower Ohmic losses, Case 2 demonstrated significant improvements in concentration uniformity, particularly at low state-of-charge (SOC) levels. The obstacle design mitigated local depletion of active species, thereby enhancing limiting current density and improving minimum concentration values across the studied SOC range. However, the introduction of obstacles increased flow resistance and pressure drops, indicating a trade-off between electrochemical performance and pumping energy requirements. Notably, Case 2 performed better at lower flow rates, showcasing its potential to optimize efficiency under varying operating conditions. At higher flow rates, the advantages of Case 2 diminished but remained evident, with better concentration uniformity, higher minimum concentration values, and a 1% average increase in limiting current density. Future research should focus on optimizing obstacle geometry and positioning to further enhance performance.

**Keywords:** organic redox flow battery; numerical model; concentration uniformity; limiting current density; pressure drop



Academic Editors: Chris Mi, Zhi Cao and Naser Vosoughi Kurdkandi

Received: 14 December 2024

Revised: 9 January 2025

Accepted: 11 January 2025

Published: 16 January 2025

**Citation:** Martínez-López, J.; Fernández-Gamiz, U.; Sánchez-Díez, E.; Beloki-Arondo, A.;

Ortega-Fernández, Í. Enhancing Mass Transport in Organic Redox Flow Batteries Through Electrode Obstacle Design. *Batteries* **2025**, *11*, 29.

<https://doi.org/10.3390/batteries11010029>

**Copyright:** © 2025 by the authors. Licensee MDPI, Basel, Switzerland. This article is an open access article distributed under the terms and conditions of the Creative Commons Attribution (CC BY) license (<https://creativecommons.org/licenses/by/4.0/>).

## 1. Introduction

The energy scene is transforming into one moving toward a sustainable future. Renewable resources such as solar and wind are considered cleaner substitutes for fossil fuel, yet their intermittency and unpredictability introduce significant challenges toward grid stability [1,2]. While energy systems are evolving and incorporating increasing shares of variable renewable energy resources, energy storage solutions will be important to maintain the balance between supply and demand and ensure reliability to accomplish a successful energy transition [3,4]. Energy storage will play one of the leading roles in this transition, allowing energy to be captured and provided later at needed times. Among the different storage systems developed, redox flow batteries (RFBs) have emerged as one of the most promising technologies for wide application because of their modular design,

scalability, and flexibility [5,6]. Unlike traditional batteries, RFBs allow independent scaling of storage capacity and power output due to the separation of the energy storage and power conversion components [7,8]. This feature makes them extremely suitable for grid-scale applications and integration with renewable energy sources.

Among the variants of RFBs, vanadium-based RFBs (VRFBs) are the most commercially developed technology [9]. These VRFBs have demonstrated promising performance in terms of long cycle life, chemical stability, and grid-scale deployments [10,11]. However, VRFBs also have their own challenges, such as the energy density being limited by the solubility constraints of vanadium species, and their reliance on vanadium, a critical metal with price and supply uncertainties [12,13]. Limitations in the existing systems has led to researchers exploring other chemistries such as organic redox flow batteries (ORFBs). This includes using organic active species derived from abundant elements in the Earth's crust to reduce some drawbacks in VRFBs. These molecules provide a sustainable solution for the substitution of inorganic compounds with environmentally more benign materials [14,15]. These systems provide multiple advantages, like higher solubility, tunability, and the potential for cost reduction, and hence, may lead to better sustainability and efficiency in energy storage [16].

In the area of organic redox chemistry, significant progress has been achieved in alkaline systems. Lin et al. [17] presented the synergy between 2,6-dihydroxyanthraquinone (2,6 DHAQ) as a negative electrolyte and ferricyanide ( $[\text{Fe}(\text{CN})_6]^{4-} / [\text{Fe}(\text{CN})_6]^{3-}$ ) as a positive counterpart. This configuration enabled the achievement of power densities of  $0.45 \text{ W cm}^{-2}$  at room temperature and  $0.7 \text{ W cm}^{-2}$  at  $45 \text{ }^\circ\text{C}$ . Other researchers have confirmed the effectiveness of anthraquinones and ferricyanides as excellent alternatives [18–20]. Other chemistries have furthered the state of the art in alkaline RFBs. Zou et al. [21] reported an S/Fe RFB with a remarkable volumetric capacity of  $40.74 \text{ Ah L}^{-1}$  that can achieve 99% coulombic efficiency and maintain an extremely low capacity fade of 0.0166% per cycle. Recent work has shown that Fe/Mn-based alkaline batteries have promise for sustainable energy storage. Shen et al. [22] reported a theoretical cell voltage of 1.43 V with close to ideal coulombic efficiency over 400 cycles; however, there was a gradual drop in voltage efficiency from 75.3% to 61.4%.

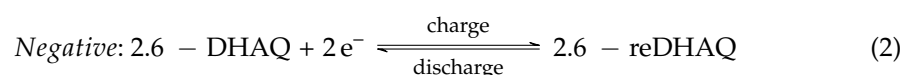
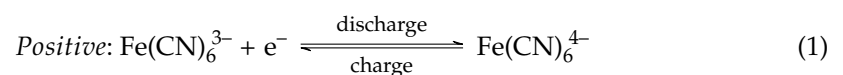
While experimental approaches provide critical insights, their high resource demands have shifted attention toward computational methods. Within these, computational fluid dynamics (CFD) has proved capable of modeling electrochemical devices successfully [23]. In this framework, numerous studies have been conducted to enhance mass transport using numerical simulations [24,25]. Pan et al. [26] applied a gradient decrease from the inlet to the outlet in channel width. The uniformity of active species was improved, which translated to higher power density and reduced polarization losses. Martinez-Lopez et al. [27] investigated the impact of electrode compression in convection using a 2D numerical model. Their findings revealed that applying 50% compression enhanced velocity profiles by 12.7%. Xu et al. [28] utilized a different distributor within a detailed 3D model. They evaluated the batteries both with and without a flow field and with serpentine and parallel patterns. They studied the performance metrics, overpotentials, pressure drops, and uniformity along the distributor, including a sensitivity analysis on the flow rate. Xu et al. also gave an overall efficiency metric for each geometry and then concluded that the serpentine flow pattern had a better performance and efficiency. Chu et al. [29] introduced a 3D numerical model utilizing 2,6-dihydroxyanthraquinone and ferrocyanide electrolytes, focusing on the effects of various electrode geometries, such as rectangular, trapezoidal, and sector shapes, on performance metrics like voltage, overpotentials, and efficiency. The sector-shaped electrode configuration showed the best results in mass transfer and power-based efficiency. Aparicio-Mauricio et al. [30] explored the influence

of manifold design on electrolyte distribution, showing that uneven flow from dividing manifolds led to increased shear stress, higher pressure drops, and performance losses, including elevated voltage and current density deviations. Akuzum et al. [31] investigated the effects of channel obstructions and ramps on mass transport. They found that a ramped channel design enhances electrochemical performance by increasing electrolyte penetration at the electrode–membrane interface. However, adding obstructions worsened performance due to electrolyte bypassing. Notably, both tapered and obstructed channels result in lower pressure drops compared to an unmodified flow field. Messaggi et al. [32] studied the effects of obstruction placement on the flow channels. Results showed that electrolyte penetration was enhanced when the obstructions were placed on the channel side, whereas those placed at the electrode interface direct electrolyte better toward the channel outlet. Biomimetic flow fields inspired by leaf veins were proposed for VRFBs to improve electrolyte distribution by Liu et al. [33]. Among the designs, circular obstacles in the main channel achieved the best performance, with enhanced voltage efficiency and concentration uniformity, offering a promising approach for practical applications. The use of static mixers along variable compression has also been studied to improve performance on flow-through configurations [34,35]. The reactant distribution is shown to be enhanced, translating to cell voltage improvement, reduction of concentration overpotential and extended capacity.

Previous research has predominantly concentrated on flow-by configuration VRFBs, and the limited research on organic redox flow batteries has focused on clarifying the influence of electrode construction and manifold configuration. This work aims to expand the knowledge on the effects of introducing obstacles on flow-through configuration batteries. To address this gap, a two-dimensional stationary isothermal model is developed to analyze obstacle placement compared to a baseline design under different working conditions. The study evaluates the impact on discharge voltage, limiting current density, concentration uniformity, and pressure drop across different states of charge (SOC) and flow rates.

## 2. Model Description

A schematic representation of the ORFB is shown in Figure 1. The electrolytes are kept in two separate reservoirs. The  $([\text{Fe}(\text{CN})_6]^{4-}/[\text{Fe}(\text{CN})_6]^{3-})$  redox pair is stored in the posolyte tank, while 2,6 dihydroxyanthraquinone (2,6 DHAQ)/2,6 reduced DHAQ is stored in the negolyte tank. The electrolyte is circulated to the porous electrodes, which act as active sites for the electrochemical reactions, via peristaltic pumps during battery operation. An ion-selective membrane is placed between the electrodes, which allows only selected ions to flow through while preventing cross-contamination. The following electrochemical processes are taking place on the cathode and anode surfaces:



A two-dimensional cell model has been developed for this work, which includes three domains: the cathode, the ion exchange membrane, and the anode. The key assumptions to reduce the complexity of the multiphysics behavior of the battery taken into consideration are:

- The model is stationary.
- Every property of the electrode and membrane is isotropic.
- It is assumed that the entire cell is isothermal.

- The electrolyte is considered incompressible.
- There is no modeling of parasitic reactions.
- Infinite dilute approximation is considered.
- The membrane only permits  $K^+$  ions to pass through. All other ion crossover is disregarded.

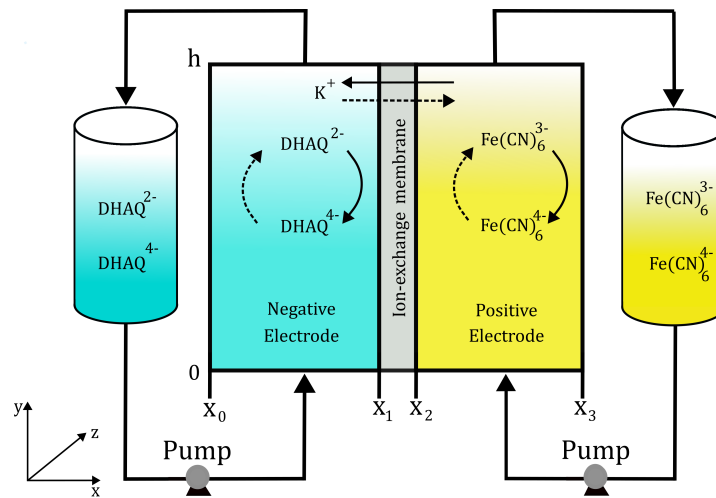


Figure 1. Schematic representation of the numerical model.

The concept of obstacle placement compared to a base case is shown in Figure 2. The obstacles are rectangular prisms.

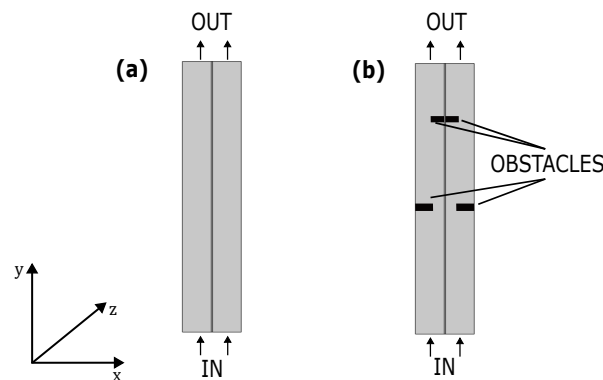


Figure 2. Schematic representation of the (a) typical no-obstacle flow-through configuration and (b) the proposed obstacle configuration.

### 2.1. Governing Equations

#### 2.1.1. Mass Transport

The conservation of mass for each species  $i$  is expressed by Equation (3):

$$\frac{\partial}{\partial t}(\epsilon c_i) + \nabla \cdot \mathbf{N}_i = -S_i \tag{3}$$

where  $c$  denotes the concentration of species  $i$ ,  $\epsilon$  denotes the electrode porosity, and  $S$  stands for the source term of each substance  $i$ , provided in Table 1.

Table 1. Source terms of species.

Species	Positive Electrode	Negative Electrode
$[Fe(CN)_6]^{4-}$	$i_r/F$	-
$[Fe(CN)_6]^{3-}$	$-i_r/F$	-
$DHAQ^{2-}$	-	$2i_r/F$
$DHAQ^{4-}$	-	$-2i_r/F$

The Nernst–Planck equation expresses the flux of charged species by diffusion, migration, and convection, represented as  $\mathbf{N}_i$ :

$$\mathbf{N}_i = -D_i^{eff} \nabla c_i - z_i u_i c_i F \nabla \phi_l + \mathbf{u} c_i \quad (4)$$

where  $D_i^{eff}$  is the effective diffusivity,  $z$  stands for the charge of species,  $u$  indicates ionic mobility,  $F$  represents the Faraday constant, and  $\phi_l$  is the liquid phase potential.  $\mathbf{u}$  indicates the electrolyte velocity. Table 2 provides a summary of electrolyte characteristics.

**Table 2.** Properties of electrolyte.

Quantity	Symbol	Value	References
Diffusivity of $[\text{Fe}(\text{CN})_6]^{4-}$	$D_{[\text{Fe}(\text{CN})_6]^{4-}}$	$8.2 \times 10^{-10} \text{ m}^2 \text{ s}^{-1}$	[36]
Diffusivity of $[\text{Fe}(\text{CN})_6]^{3-}$	$D_{[\text{Fe}(\text{CN})_6]^{3-}}$	$8.6 \times 10^{-10} \text{ m}^2 \text{ s}^{-1}$	[36]
Diffusivity of $\text{DHAQ}^{2-}$	$D_{\text{DHAQ}^{2-}}$	$4.8 \times 10^{-10} \text{ m}^2 \text{ s}^{-1}$	[17]
Diffusivity of $\text{DHAQ}^{4-}$	$D_{\text{DHAQ}^{4-}}$	$4.8 \times 10^{-10} \text{ m}^2 \text{ s}^{-1}$	[17]
Diffusivity of $\text{K}^+$	$D_{\text{K}^+}$	$1.96 \times 10^{-9} \text{ m}^2 \text{ s}^{-1}$	[37]
Diffusivity of $\text{OH}^-$	$D_{\text{OH}^-}$	$5.2 \times 10^{-9} \text{ m}^2 \text{ s}^{-1}$	[37]

$D_i^{eff}$  is obtained by means of the Bruggemann correlation:

$$D_i^{eff} = \varepsilon^{3/2} D_i \quad (5)$$

The Nernst–Einstein equation is used to calculate ionic mobility:

$$u_i = \frac{D_i^{eff}}{RT} \quad (6)$$

where  $R$  refers to the universal gas constant and  $T$  is the temperature.

Darcy’s Law is used for the convection term in porous electrodes:

$$\mathbf{u} = -\frac{K}{\mu} \nabla p \quad (7)$$

where  $K$  stands for the porous electrode permeability,  $\mu$  is the dynamic viscosity of electrolyte, and  $p$  refers to pressure. The following is the Kozeny–Carman equation for permeability:

$$K = \frac{d_f^2 \varepsilon^3}{16 k_{ck} (1 - \varepsilon)^2} \quad (8)$$

where  $d_f$  stands for the electrode fiber diameter and  $k_{ck}$  is the Kozeny–Carman constant, listed with additional electrode parameters in Table 3.

**Table 3.** Electrode parameters.

Quantity	Symbol	Value	References
Non-compressed electrode porosity	$\varepsilon$	0.895	[38]
Non-compressed electrode specific surface area	$a$	$3.5 \times 10^4 \text{ m}^2 \text{ m}^{-3}$	Fitted
Non-compressed electrode conductivity	$\sigma_s$	$66.7 \text{ S m}^{-1}$	[39]
Kozeny–Carman constant	$K_{ck}$	4.28	[40]

Since only  $\text{K}^+$  ions are permitted to pass through the membrane, the ion flux is determined by:

$$\mathbf{N}_{\text{K}^+} = -\frac{\sigma_{mem}}{F} \Delta \phi_{mem} \quad (9)$$

where the potential and membrane conductivity are denoted by  $\phi_{mem}$  and  $\sigma_{mem}$ , respectively.

### 2.1.2. Reaction Kinetics

The electrochemical reactions at the electrode surface are modeled using the Butler–Volmer model:

$$i_{r,pos} = i_{0,pos}a \left[ \exp\left(\frac{(1-\alpha_{pos})F\eta_+}{RT}\right) - \exp\left(\frac{(-\alpha_{pos})F\eta_+}{RT}\right) \right] \quad (10)$$

$$i_{r,neg} = i_{0,neg}a \left[ \exp\left(\frac{(1-\alpha_{neg})F\eta_-}{RT}\right) - \exp\left(\frac{(-\alpha_{neg})F\eta_-}{RT}\right) \right] \quad (11)$$

The positive and negative reaction rates are denoted by the terms  $i_{r,pos}$  and  $i_{r,neg}$ , respectively. Specific surface area of the porous electrode is denoted by  $a$ ,  $\eta_+$  and  $\eta_-$  are the positive and negative overpotential, charge transfer coefficients for positive and negative reactions are denoted by  $\alpha_{pos}$  and  $\alpha_{neg}$ , and exchange current density  $i_{0,pos}$  and  $i_{0,neg}$  are determined by:

$$i_{0,pos} = Fk_{pos}(c_{[Fe(CN)_6]^{3-}})^{1-\alpha_{pos}}(c_{[Fe(CN)_6]^{4-}})^{\alpha_{pos}} \quad (12)$$

$$i_{0,neg} = Fk_{neg}(c_{DHAQ^{2-}})^{1-\alpha_{neg}}(c_{DHAQ^{4-}})^{\alpha_{neg}} \quad (13)$$

where the reaction rate constants for the positive and negative sides are denoted by  $k_{pos}$  and  $k_{neg}$ , respectively.

The following formulas can be used to determine the overpotential of the positive and negative electrodes:

$$\eta_+ = \varphi_s - \varphi_l - E_{eq,+} \quad (14)$$

$$\eta_- = \varphi_s - \varphi_l - E_{eq,-} \quad (15)$$

where  $\varphi_s$  represents the solid phase potential, and  $E_{eq,+}$  and  $E_{eq,-}$  denote open circuit potentials of positive and negative reactions, respectively. These potentials can be obtained using the Nernst equation:

$$E_{eq,+} = E'_{eq,+} + \frac{RT}{F} \ln \left( \frac{c_{[Fe(CN)_6]^{3-}}}{c_{[Fe(CN)_6]^{4-}}} \right) \quad (16)$$

$$E_{eq,-} = E'_{eq,-} + \frac{RT}{2F} \ln \left( \frac{c_{DHAQ^{2-}}}{c_{DHAQ^{4-}}} \right) \quad (17)$$

where  $E'_{eq,+}$  and  $E'_{eq,-}$  indicate the standard equilibrium potentials for the positive and negative side reactions, outlined in Table 4 alongside the other kinetic parameters.

**Table 4.** Kinetic parameters

Quantity	Symbol	Value	References
Standard equilibrium potential for positive reaction	$E'_{eq,+}$	0.33 V	[29]
Standard equilibrium potential for negative reaction	$E'_{eq,-}$	−0.71 V	[29]
Cathodic transfer coefficient	$\alpha_{pos}$	0.5	[17]
Anodic transfer coefficient	$\alpha_{neg}$	0.5	[17]
Rate constant for positive reaction	$k_{pos}$	$6 \times 10^{-7} \text{ m s}^{-1}$	[29]
Rate constant for negative reaction	$k_{neg}$	$7 \times 10^{-7} \text{ m s}^{-1}$	[29]

### 2.1.3. Charge Conservation

The principle of electroneutrality requires that the total charge in the electrolyte equals zero, ensuring electrical neutrality:

$$\sum_i z_i c_i = 0 \quad (18)$$

To satisfy charge conservation, current flow in the solid and liquid phases is coupled with electrochemical reactions through the following equation:

$$\nabla \cdot \mathbf{i}_l = -\nabla \cdot \mathbf{i}_s = \mathbf{i}_r \quad (19)$$

which implies that the current leaving the electrolyte,  $\mathbf{i}_l$ , matches the current entering the electrode,  $\mathbf{i}_s$ , and collectively equals the electrochemical reaction rate,  $\mathbf{i}_r$ . The solid and liquid phase currents are expressed as follows:

$$\mathbf{i}_s = -\sigma_s^{eff} \nabla \varphi_s \quad (20)$$

$$\mathbf{i}_l = F \sum_i z_i \mathbf{N}_i \quad (21)$$

where  $\sigma_s^{eff}$  represents the effective conductivity of the electrode, determined using the bulk conductivity of the electrode material,  $\sigma_s$ , and calculated as follows:

$$\sigma_s^{eff} = (1 - \varepsilon)^{3/2} \sigma_s \quad (22)$$

#### 2.1.4. Boundary Conditions

Boundary conditions are defined using the  $x$  and  $y$  coordinates shown in Figure 1. At the external boundary of the anode, located at  $x = x_0$ , the solid potential is set to zero by grounding this boundary:

$$\varphi_s = 0 \quad \text{at} \quad x = x_0 \quad (23)$$

At the cell's lower boundary,  $y = 0$ , the species inlet flux is defined based on the flow rate  $Q$ , electrode width  $w_e$ , and electrode thickness  $t_e$ :

$$\mathbf{n} \cdot \mathbf{u} = \frac{Q}{\varepsilon w_e t_e} \quad \text{at} \begin{cases} x_0 < x < x_1 & \text{and} & x_2 < x < x_3 \\ y = 0 \end{cases} \quad (24)$$

The species concentration at the electrode inlet remains constant:

$$c_i = c_i^{in} \quad \text{at} \begin{cases} x_0 < x < x_1 & \text{and} & x_2 < x < x_3 \\ y = 0 \end{cases} \quad (25)$$

At all other boundaries, the mass flux is zero, with the exception of  $K^+$  at the membrane–electrode interface:

$$-\mathbf{n} \cdot \mathbf{N}_i = 0 \quad \text{at} \begin{cases} y = 0 < y < y = h \\ \text{for} \\ x = (x_0, x_1, x_2, x_3) \end{cases} \quad (26)$$

Here,  $h$  represents the height of the cell. At this location, a pressure outlet is defined:

$$p = p_{out} \quad \text{at} \begin{cases} x_0 < x < x_1 & \text{and} & x_2 < x < x_3 \\ y = h \end{cases} \quad (27)$$

and the diffusive flux of all species is neglected:

$$-D_i^{eff} \nabla c_i \cdot \mathbf{n} = 0 \quad \text{at} \begin{cases} x_0 < x < x_1 & \text{and} & x_2 < x < x_3 \\ y = h \end{cases} \quad (28)$$

At the membrane–electrode interface, charge continuity is maintained by defining the continuity of the electrolyte current density to the current density in the membrane:

$$\mathbf{n} \cdot \mathbf{i}_1 = \mathbf{n} \cdot \mathbf{i}_{1,\text{mem}} \quad \text{at} \begin{cases} y = 0 < y < y = h \\ \text{for} \\ x = (x_1, x_2) \end{cases} \quad (29)$$

The top and bottom edges of both the membrane and electrodes are electrically insulated:

$$\begin{cases} -\mathbf{n} \cdot \mathbf{i}_1 = 0 \\ -\mathbf{n} \cdot \mathbf{i}_s = 0 \end{cases} \begin{cases} x_0 < x < x_3 \\ y = 0 \quad \text{and} \quad y = h \end{cases} \quad (30)$$

A constant current density, controlled by the user, is applied to the external boundary of the positive electrode:

$$\mathbf{n} \cdot \mathbf{i}_s = i_{\text{avg}} \quad \text{at} \quad x = x_3 \quad (31)$$

All geometric and operational parameters are provided in Table 5.

**Table 5.** Geometrical and operation parameters.

Quantity	Symbol	Value	References
Electrode length	$h$	0.04 m	[38]
Non-compressed electrode thickness	$t_e$	0.006 m	[38]
Electrode width	$w_e$	0.04 m	[38]
Membrane thickness	$t_m$	0.000183 m	[38]
Flow rate	$Q$	60 mL min <sup>-1</sup>	-
Temperature	$T$	298 K	-
Outlet pressure	$p_{\text{out}}$	0 Pa	-
State of Charge	$SOC$	50%	-

## 2.2. Battery Performance Parameters

The concentration of each species is determined based on the user-defined parameter SOC, with the total concentrations on the positive and negative sides denoted as  $c_1$  and  $c_0$ , respectively:

$$c_{\text{reDHAQ}} = c_0 \cdot SOC \quad (32)$$

$$c_{\text{DHAQ}} = c_0 \cdot (1 - SOC) \quad (33)$$

$$c_{\text{Fe}(\text{CN})_6^{4-}} = c_1 \cdot (1 - SOC) \quad (34)$$

$$c_{\text{Fe}(\text{CN})_6^{3-}} = c_1 \cdot SOC \quad (35)$$

A crucial factor in assessing species distribution is the uniformity factor, which measures how evenly a species is spread throughout the system. It quantifies the concentration variation of species  $i$  and is calculated as follows:

$$U_i = 1 - \frac{1}{c_{i,\text{avg}}} \sqrt{\frac{1}{V} \iiint (c_i - c_{i,\text{avg}})^2 dV} \quad (36)$$

where  $c_{i,\text{avg}}$  denotes the average concentration of species  $i$ , and  $V$  represents the volume of the electrode.

## 2.3. Numerical Model

The simulation model was created using COMSOL Multiphysics 5.5. For the positive and negative electrodes, the Tertiary Current Distribution module was utilized, while the Secondary Current Distribution module was applied to the membrane. The fluid dynamics equations within the porous electrodes were addressed using the Brinkman equations, solved via a finite volume method. The PARDISO solver was selected, with a convergence criterion of  $1 \times 10^{-6}$  relative error to ensure high precision in the results. To optimize



computational efficiency while maintaining accuracy, a mesh independence study was carried out, demonstrating that grid refinements beyond 3100 elements did not significantly alter the outcomes, as shown in Figure 3.

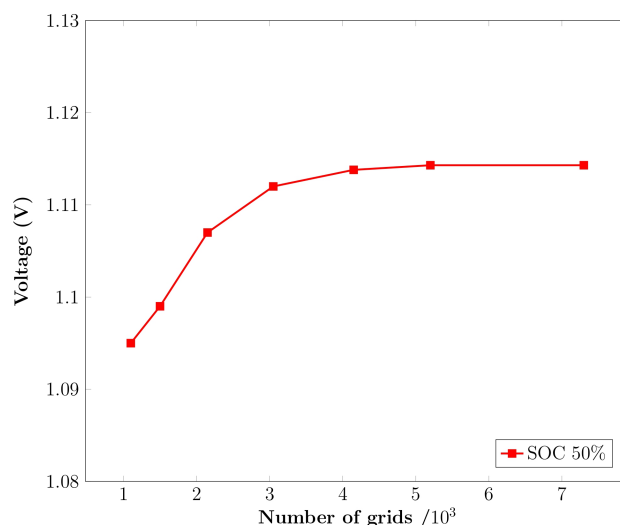


Figure 3. Grid dependency study.

### 3. Results

#### 3.1. Experimental Validation

To validate the numerical model, the results were compared with experimental data from Chu et al. [29], using a rectangular electrode with dimensions of 20 mm × 20 mm × 3.5 mm. The flow rate of the circulation pump was set to 60 ml min<sup>-1</sup>, with a current density of 40 mA cm<sup>-2</sup>, and a Nafion 212 cation exchange membrane was used as the ion-exchange medium. In these tests, the concentration of the positive active material was 200 mol m<sup>-3</sup>, while the concentration of the negative active material was 100 mol m<sup>-3</sup>. Figure 4 presents the cell potential during charge and discharge modes for both experimental and numerical models. The maximum error, which occurs at the endpoints of the charge-discharge curves, remained below 3.6%, with an average error of 1.45%, confirming the accuracy and reliability of the numerical model for subsequent analysis.

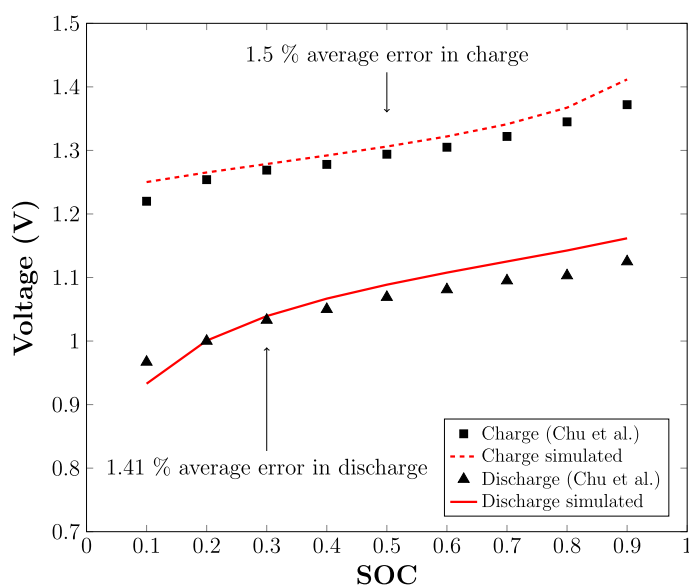


Figure 4. Results of experimental validation [29].

### 3.2. Case Studies

Two configurations were investigated to assess the influence of obstacle placement. Case 1 serves as the baseline, with no obstacles incorporated, providing a reference for evaluating the effects of the modified configuration. In Case 2, obstacles are introduced within the electrode structure. Two obstacles are introduced in each electrode, both obstructing 50% of the electrode thickness. One is located at the electrode outer boundary, and the second is placed at the electrode membrane interface. All obstacles have a dimension of 1 mm in electrolyte flow direction. The obstacle at the outer boundary is located at one-third of the electrode length, and the other one at two-thirds of the electrode length.

For both configurations, the concentration of active material in the positive and negative compartments is set to 400 and 200 mol m<sup>-3</sup>, respectively. Additionally, the concentrations of K<sup>+</sup> and OH<sup>-</sup> ions are maintained at 1000 mol m<sup>-3</sup> on both sides.

### 3.3. Effects of SOC

Looking at Figure 5, discharge curves for Case 1 and 2 can be analyzed. The discharge curves reveal that Case 1 consistently exhibits a slightly higher voltage, 0.18% on average, compared to Case 2 across the entire range of state of charge. This behavior indicates that the baseline configuration benefits from a more direct flow path for the electrolyte, minimizing the hydraulic resistance and associated pressure drop. In contrast, the inclusion of obstacles in Case 2 leads to additional flow resistance and localized pressure gradients, which may impede uniform electrolyte penetration. However, when looking at the lower end of the SOC range, the difference between Case 1 and 2 decreases to 0.07%, see the zoom in Figure 5. While the obstacle configuration aims to enhance mass transport and mitigate concentration gradients by promoting better mixing, these potential advantages appear offset by the increased Ohmic polarization effects.

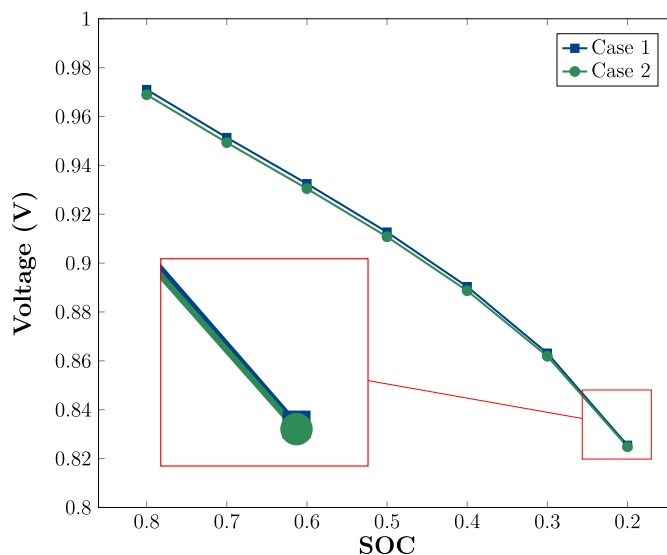


**Figure 5.** Discharge curves obtained for a flow rate of 60 mL min<sup>-1</sup> and 50 mA cm<sup>-2</sup>.

Despite the slightly lower discharge voltage observed in Case 2, this configuration demonstrates significant improvements in terms of concentration uniformity and minimum species concentration, as depicted in Figure 6a,b. Across the entire SOC range, Case 2 demonstrates a higher concentration uniformity factor compared to the baseline Case 1, which indicates enhanced distribution of active species within the electrode, see Figure 6a. For a SOC value of 0.2, Case 1 achieves a value of 88.7%, while for Case 2, this rises to 90.1%. The obstacles actually help spread electrolyte more evenly through the electrode, which prevents troublesome zones with low concentration. Though the advantage in

concentration uniformity narrows as SOC increases, the design in Case 2 still provides better distribution than in Case 1, reinforcing stable electrochemical reactions across varying SOC conditions. One potential explanation for this trend is that at lower SOC, the availability of reactants throughout the electrolyte is significantly limited, leading to pronounced concentration gradients across the cell. Under these conditions, reactant depletion near the electrode surface becomes a critical issue, particularly in regions where the flow is less effective at replenishing the consumed species. This is the operating point where obstacles can force portions of the electrolyte flow into regions that might otherwise receive minimal reactant supply, promoting a more uniform utilization of the electrode area. For higher SOC, this becomes less critical and obstacles seem to be less effective. Furthermore, the higher minimum concentration observed in Figure 6b highlights the improved utilization of active species in Case 2. This suggests that the presence of obstacles mitigates stagnant regions and optimizes mass transport.

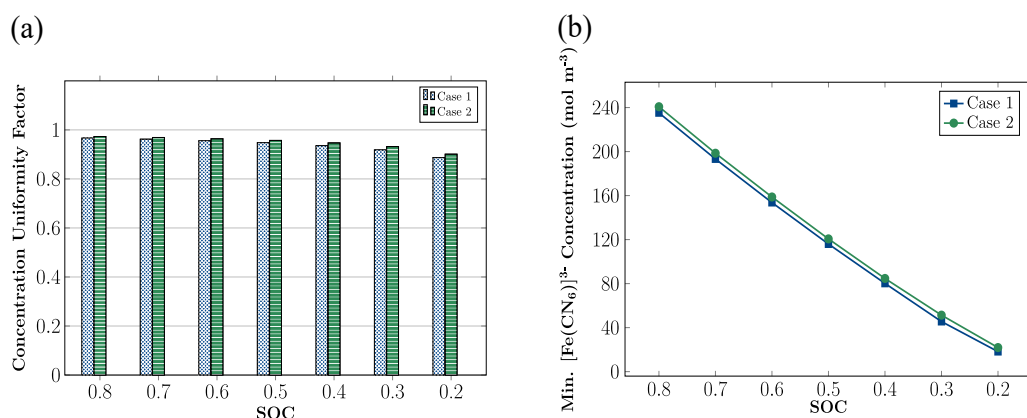


**Figure 6.** The (a) concentration uniformity factor and (b) minimum concentration of  $[\text{Fe}(\text{CN}_6)]^{3-}$  in the positive electrode for a flow rate of  $60 \text{ mL min}^{-1}$  and  $50 \text{ mA cm}^{-2}$ .

Better electrolyte distribution translates into higher limiting current density, see Figure 7. This improvement can be attributed to effectively reducing concentration gradients and mitigating localized depletion of active species. The more uniform concentration profile in Case 2, as illustrated in Figure 6a, corroborates this observation, as a well-distributed reactant supply ensures that the electrode regions farther from the inlet remain reactive even at higher current densities, even at near discharged state.

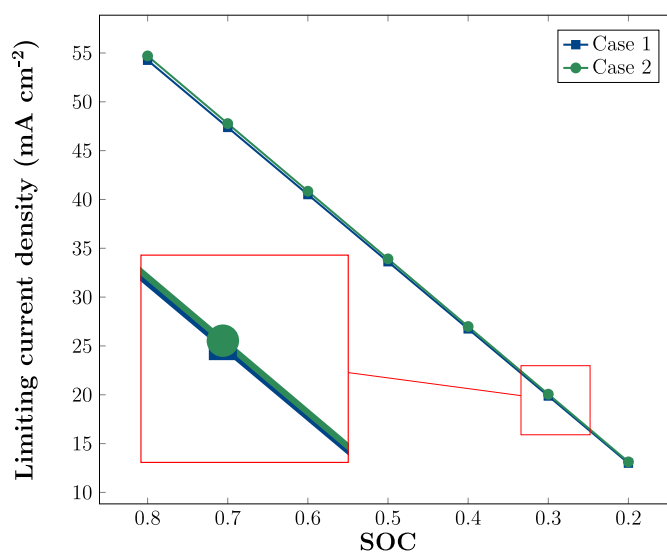


**Figure 7.** Limiting current density for a flow rate of  $60 \text{ mL min}^{-1}$  and  $50 \text{ mA cm}^{-2}$ .

### 3.4. Effects of Flow Rate

A key consideration in evaluating the effectiveness of electrode design modifications is the associated pressure drop, see Figure 8, as it directly impacts the pumping energy required for system operation. In the case of obstacle placement (Case 2), a higher pressure drop is observed compared to Case 1, by an average of 14%. The increased hydraulic resistance in Case 2 can be attributed to the obstacles interrupting the electrolyte flow path, creating regions of recirculation, while these flow dynamics improve electrolyte penetration and mixing, as seen in the higher concentration uniformity and elevated limiting current density, they simultaneously impose a penalty on pumping efficiency. This trade-off highlights a challenge on optimizing the electrode structure to enhance electrochemical performance while minimizing the energy costs associated with fluid transport.

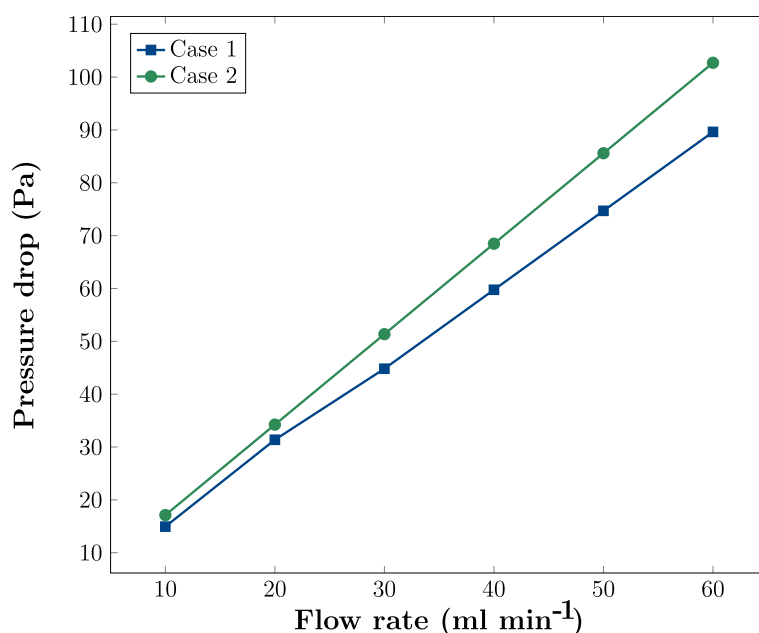


**Figure 8.** Pressure drop values for a State of Charge of 50% and 50 mA cm<sup>-2</sup> in discharge mode.

Regardless of the increase in pressure drop for Case 2, improvements in other metrics are obtained. Figure 9a shows the relation between concentration uniformity factor and flow rate for both configurations. Both curves exhibit a rising trend as the flow rate increases, reflecting enhanced reactant distribution across the electrode. However, there are notable differences in their behavior. Case 2 demonstrates a 1.8% improvement in concentration uniformity for the lowest flow rate of 10 mL min<sup>-1</sup>, and it maintains higher values across the studied range. However, this difference shrinks as the flow rate increases, down to 1.0% for 60 mL min<sup>-1</sup>. Looking at Figure 9b, benefits in minimum concentration are observed. Case 2 obtains higher minimum concentration values across the studied range, averaging a 15% increase, which translates to reduced local reactant depletion. Thanks to reducing local reactant depletion, limiting current density is raised, see Figure 10, by an average of 1% over the whole range. It is worth noting that when zooming in on Figure 10, even at lower flow rates, Case 2 consistently outperforms Case 1.

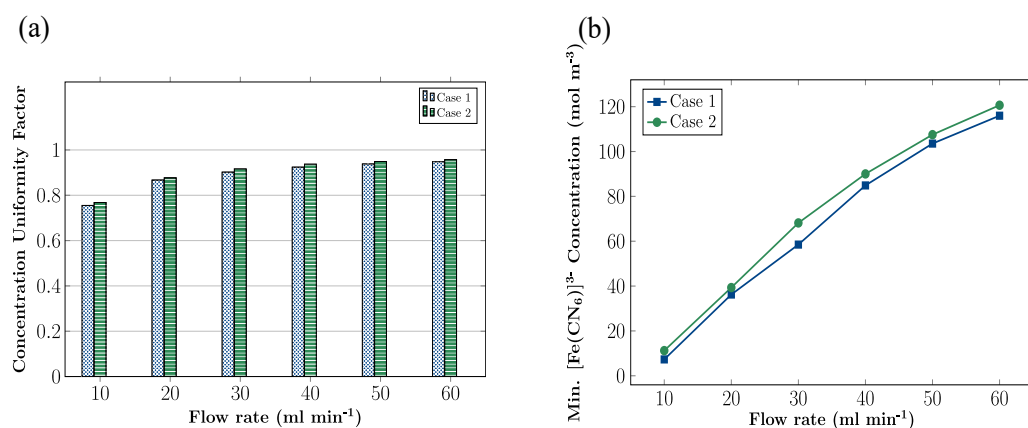


**Figure 9.** The (a) concentration uniformity factor and (b) minimum concentration of  $[\text{Fe}(\text{CN}_6)]^{3-}$  in the positive electrode for a State of Charge of 50% and  $50 \text{ mA cm}^{-2}$ .

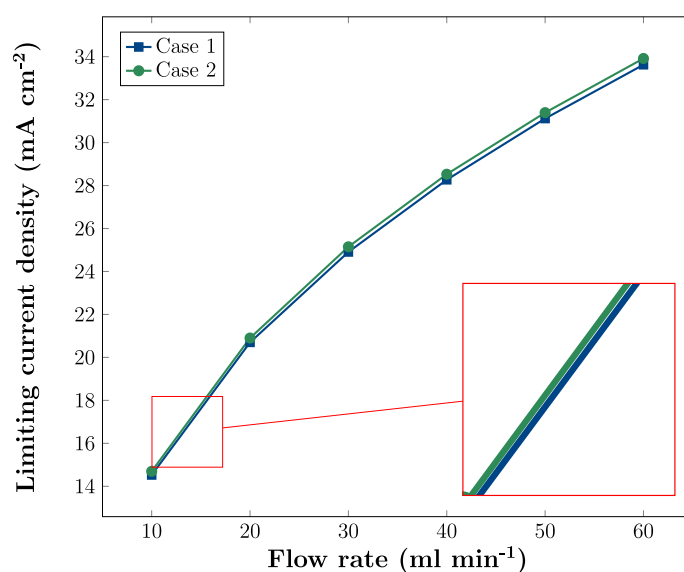


**Figure 10.** Limiting current density for a State of Charge of 50% and  $50 \text{ mA cm}^{-2}$ .

#### 4. Conclusions

In this work, the effect of placing obstacles in the electrode structure of an organic redox flow battery on reactant distribution and local depletion is investigated. Two configurations were studied: Case 1 was designated as the control without obstacles, while Case 2 featured a design with obstacles to improve mass transport and uniformity.

Analyzing the discharge profiles, it is noted that Case 1 maintained a marginally higher voltage compared to Case 2 throughout the complete state-of-charge range; the average difference was about 0.18%. Such a voltage difference can be explained due to the fact that Case 1 had a simpler flow channel leading to lower hydraulic resistance and smaller pressure drops. Conversely, the obstacles in Case 2 introduced more resistance to the flow, which consequently generated localized pressure gradients. Additionally, obstacle placement means reducing electrode area, which translates to lower electronic conductivity and increased Ohmic polarization. However, this disadvantage was compensated at lower SOC values, where the gap in performance between the two configurations narrowed considerably. Although the discharge voltage was marginally lower in Case 2, there were marked improvements in the concentration uniformity and minimum concentration of active species with this configuration. The distribution of reactants became much more uniform with the obstacles placed in Case 2, especially at low levels of SOC, thereby preventing areas of low concentration that could damage the cell, while the benefit of

concentration uniformity decreased with higher values of SOC, Case 2 still showed better distribution throughout the whole range.

The higher pressure drop of Case 2 is mainly due to the fact that the obstacles block electrolyte flow. This suggests a trade-off between the electrochemical performance and energy consumption: while the obstacles improved the mixing quality and reduced local depletion, the obstacles also created additional flow resistance that required more pumping energy.

Looking at the performance of the design with obstructions at different flow rates, Case 2 did better than Case 1, especially with lower flow rates. Although the advantage became smaller with an increase in flow rate, Case 2 still had better concentration uniformity and higher minimum concentration values within the studied range. Furthermore, having obstacles in Case 2 increased the limiting current density by 1% on average. Even at the lower flow rates, Case 2 showed better performance, indicating that the obstacles may enhance electrochemical efficiency at different operating conditions.

In conclusion, though the introduction of obstacles in the electrode structure increased the pressure drop, the enhanced concentration uniformity, limiting current density, and active species utilization bring huge benefits. It is indicated that obstacle placement could be a very promising strategy to optimize the performance of redox flow batteries. The introduction of strategically placed obstacles presents a simple yet scalable design modification that can be adapted to various operating conditions. Furthermore, the insights into the relationship between flow dynamics and electrochemical performance establish a foundation for future optimization efforts, including refining obstacle geometry and placement to balance improvements in mass transport with the associated pumping energy costs.

**Author Contributions:** Conceptualization, J.M.-L. and U.F.-G.; methodology, A.B.-A.; software, E.S.-D.; validation, J.M.-L. and U.F.-G.; investigation, U.F.-G.; resources, E.S.-D.; data curation, A.B.-A. and Í.O.-F.; Writing—Review and Editing, J.M.-L. and Í.O.-F.; visualization, A.B.-A.; supervision, E.S.-D.; project administration, U.F.-G.; funding acquisition, U.F.-G. All authors have read and agreed to the published version of the manuscript.

**Funding:** Government of the Basque Country: Elkartek CICE2022; KK-2022/00043 and ELKARTEK24/15, KK-2024/00035; CIEMAT: Energía eólica offshore para el ensayo y el desarrollo energético de energías renovables e hidrógeno verde; Government of the Basque Country: Mobility Lab Foundation; Government of the Basque Country: ITSAS-REM (IT1514-22).

**Data Availability Statement:** All data generated in the current study are available upon reasonable request to the corresponding author.

**Acknowledgments:** The authors are grateful for the support provided by SGIker of UPV/EHU. This research was developed under the frame of the Joint Research Laboratory on Offshore Renewable Energy (JRL-ORE).

**Conflicts of Interest:** Authors Eduardo Sánchez-Díez, Aitor Beloki-Arrondo and Íñigo Ortega-Fernández were employed by Basque Research and Technology Alliance (BRTA). The remaining authors declare that the research was conducted in the absence of any commercial or financial relationships that could be construed as a potential conflict of interest.

## Nomenclature

List of symbols

$a$	Specific surface area
$c$	Concentration
$D$	Diffusion coefficient
$d_f$	Fiber diameter

$E$	Equilibrium potential
$F$	Faraday constant
$h$	Height
$i_0$	Exchange current density
$i_r$	Electrochemical reaction rate
$K$	Permeability
$K_{ck}$	Kozeny–Carman constant
$k$	Reaction rate constant
$N$	Flux of charged species
$p$	Pressure
$Q$	Volumetric flow rate
$R$	Constant of ideal gases
$S$	Source term
$T$	Temperature
$t$	Time
$u$	Mobility
$u$	Velocity
$w$	Width
$z$	Species charge
Greek	
$\alpha$	Charge transfer coefficient
$\varepsilon$	Electrode porosity
$\eta$	Overpotential
$\varphi$	Potential
$\sigma$	Conductivity
$\mu$	Dynamic viscosity
Superscripts and subscripts	
+	Positive side
–	Negative side
'	Standard
<i>avg</i>	Average
<i>e</i>	Electrode
<i>eff</i>	Effective
<i>i</i>	Species
<i>l</i>	Liquid
<i>mem</i>	Membrane
<i>out</i>	Outlet
<i>s</i>	Solid

## Abbreviations

The following abbreviations are used in this manuscript:

CFD	Computational fluid dynamics
RFB	Redox flow battery
VRFB	Vanadium redox flow battery
ORFB	Organic redox flow battery

## References

1. Nguyen, T.; Savinell, R.F. Flow Batteries. *Electrochem. Soc. Interface* **2010**, *19*, 54. [[CrossRef](#)]
2. Asiaban, S.; Kayedpour, N.; Ebneali Samani, A.; Bozalakov, D.; De Kooning, J.; Crevecoeur, G.; Vandeveld, L. Wind and solar intermittency and the associated integration challenges: A comprehensive review including the status in the Belgian power system. *Energies* **2021**, *14*, 630. [[CrossRef](#)]
3. Mutz, M.; Perovic, M.; Gumbel, P.; Königer, V.; Taranovskyy, A.; Li, Y.; Beran, L.; Käfer, T.; Dröder, K.; Knoblauch, V.; et al. Toward a Li-Ion Battery Ontology Covering Production and Material Structure. *Energy Technol.* **2022**, *11*, 2200681. [[CrossRef](#)]

4. Braff, W.A.; Mueller, J.M.; Trancik, J.E. Value of storage technologies for wind and solar energy. *Nat. Clim. Chang.* **2016**, *6*, 964–969. [[CrossRef](#)]
5. Yu, J.; Fan, L.; Yan, R.; Zhou, M.; Wang, Q. Redox Targeting-Based Aqueous Redox Flow Lithium Battery. *ACS Energy Lett.* **2018**, *3*, 2314–2320. [[CrossRef](#)]
6. Reed, D.; Thomsen, E.; Li, B.; Wang, W.; Nie, Z.; Koeppe, B.; Kizewski, J.; Sprenkle, V. Stack Developments in a kW Class All Vanadium Mixed Acid Redox Flow Battery at the Pacific Northwest National Laboratory. *J. Electrochem. Soc.* **2015**, *163*, A5211. [[CrossRef](#)]
7. Arevalo-Cid, P.; Dias, P.; Mendes, A.; Azevedo, J. Redox flow batteries: A new frontier on energy storage. *Sustain. Energy Fuels* **2021**, *5*, 5366–5419. [[CrossRef](#)]
8. Lourenssen, K.; Williams, J.; Ahmadpour, F.; Clemmer, R.; Tasnim, S. Vanadium redox flow batteries: A comprehensive review. *J. Energy Storage* **2019**, *25*, 100844. [[CrossRef](#)]
9. Liu, Y.; Xu, J.; Lu, S.; Xiang, Y. Titanium Nitride Nanorods Array-Decorated Graphite Felt as Highly Efficient Negative Electrode for Iron-Chromium Redox Flow Battery. *Small* **2023**, *19*, e2300943. [[CrossRef](#)]
10. Cunha, A.; Martins, J.; Rodrigues, N.; Brito, F. Vanadium redox flow batteries: A technology review. *Int. J. Energy Res.* **2014**, *39*, 889–918. [[CrossRef](#)]
11. Bhattarai, A.; Whitehead, A.; Schweiss, R.; Scherer, G.; Skyllas-Kazacos, M.; Wai, N.; Nguyen, T.; Ghimire, P.; Oo, M.; Hng, H. Anomalous Behavior of Anion Exchange Membrane during Operation of a Vanadium Redox Flow Battery. *ACS Appl. Energy Mater.* **2019**, *2*, 1712–1719. [[CrossRef](#)]
12. Skyllas-Kazacos, M.; Chakrabarti, B.; Hajimolana, Y.S.; Mjalli, F.; Saleem, M. Progress in Flow Battery Research and Development. *J. Electrochem. Soc.* **2011**, *158*, R55–R79. [[CrossRef](#)]
13. Minke, C.; Kunz, U.; Turek, T. Techno-economic assessment of novel vanadium redox flow batteries with large-area cells. *J. Power Sources* **2017**, *361*, 105–114. [[CrossRef](#)]
14. Leung, P.; Shah, A.A.; Sanz, L.; Flox, C.; Morante, J.R.; Xu, Q.; Mohamed, M.R.; Ponce de León, C.; Walsh, F.C. Recent developments in organic redox flow batteries: A critical review. *J. Power Sources* **2017**, *360*, 243–283. [[CrossRef](#)]
15. Yu, L.C.; Luo, Y.C.; Feng, W.; Zhang, S.; Zhang, X. Fluorinated TEMPO: A new redox-active catholyte material for aqueous Zn-anode hybrid flow batteries. *J. Mater. Chem. A* **2023**, *11*, 18911–18921. [[CrossRef](#)]
16. Sánchez-Díez, E.; Ventosa, E.; Guarnieri, M.; Trovò, A.; Flox, C.; Marcilla, R.; Soavi, F.; Mazur, P.; Aranzabe, E.; Ferret, R. Redox flow batteries: Status and perspective towards sustainable stationary energy storage. *J. Power Sources* **2021**, *481*, 228804. [[CrossRef](#)]
17. Lin, K.; Chen, Q.; Gerhardt, M.R.; Tong, L.; Kim, S.B.; Eisenach, L.; Valle, A.W.; Hardee, D.; Gordon, R.G.; Aziz, M.J.; et al. Alkaline quinone flow battery. *Science* **2015**, *349*, 1529–1532. [[CrossRef](#)] [[PubMed](#)]
18. Huang, S.; Zhang, H.; Salla, M.; Zhuang, J.; Zhi, Y.; Wang, X.; Wang, Q. Molecular engineering of dihydroxyanthraquinone-based electrolytes for high-capacity aqueous organic redox flow batteries. *Nat. Commun.* **2022**, *13*, 4746. [[CrossRef](#)] [[PubMed](#)]
19. Peng, K.; Li, Y.; Tang, G.; Liu, Y.; Yang, Z.; Xu, T. Solvation regulation to mitigate the decomposition of 2,6-dihydroxyanthraquinone in aqueous organic redox flow batteries. *Energy Environ. Sci.* **2023**, *16*, 430–437. [[CrossRef](#)]
20. Jin, S.; Fell, E.M.; Vina-Lopez, L.; Jing, Y.; Michalak, P.W.; Gordon, R.G.; Aziz, M.J. Near Neutral pH Redox Flow Battery with Low Permeability and Long-Lifetime Phosphonated Viologen Active Species. *Adv. Energy Mater.* **2020**, *10*, 2000100. [[CrossRef](#)]
21. Zou, H.; Xu, Z.; Xiong, L.; Wang, J.; Fu, H.; Cao, J.; Ding, M.; Wang, X.; Jia, C. An alkaline S/Fe redox flow battery endowed with high volumetric-capacity and long cycle-life. *J. Power Sources* **2024**, *591*, 233856. [[CrossRef](#)]
22. Shen, X.; Kellamis, C.; Tam, V.; Sinclair, N.; Wainright, J.; Savinell, R. An All-Soluble Fe/Mn-Based Alkaline Redox Flow Battery System. *ACS Appl. Mater. Interfaces* **2024**, *16*, 18686–18692. [[CrossRef](#)]
23. Aramendia, I.; Fernandez-Gamiz, U.; Martinez-San-Vicente, A.; Zulueta, E.; Lopez-Guede, J.M. Vanadium Redox Flow Batteries: A Review Oriented to Fluid-Dynamic Optimization. *Energies* **2021**, *14*, 176. [[CrossRef](#)]
24. Esan, O.C.; Shi, X.; Pan, Z.; Huo, X.; An, L.; Zhao, T. Modeling and Simulation of Flow Batteries. *Adv. Energy Mater.* **2020**, *10*, 2000758. [[CrossRef](#)]
25. Sun, J.; Guo, Z.; Pan, L.; Fan, X.; Wei, L.; Zhao, T. Redox flow batteries and their stack-scale flow fields. *Carbon Neutrality* **2023**, *2*, 30. [[CrossRef](#)]
26. Pan, L.; Xie, J.; Guo, J.; Wei, D.; Qi, H.; Rao, H.; Leung, P.; Zeng, L.; Zhao, T.; Wei, L. In-plane gradient design of flow fields enables enhanced convections for redox flow batteries. *Energy Adv.* **2023**, *2*, 2006–2017. [[CrossRef](#)]
27. Martinez Lopez, J.; Aramendia, I.; Fernandez-Gamiz, U.; Sanchez-Diez, E.; Beloki, A.; Kurt, E.; Lopez-Guede, J.M. Computational Modeling of a 2D Vanadium Redox Flow Battery Cell. *JOM* **2024**, *76*, 130–140. [[CrossRef](#)]
28. Xu, Q.; Zhao, T.S.; Leung, P.K. Numerical investigations of flow field designs for vanadium redox flow batteries. *Appl. Energy* **2013**, *105*, 47–56. [[CrossRef](#)]
29. Chu, F.; Su, M.; Xiao, G.; Tan, Z.; Yang, G. Analysis of Electrode Configuration Effects on Mass Transfer and Organic Redox Flow Battery Performance. *Ind. Eng. Chem. Res.* **2022**, *61*, 2915–2925. [[CrossRef](#)]



30. Aparicio-Mauricio, G.; Jiménez-Lima, L.; Rivero, E.P.; Cruz-Díaz, M.R. 3D modeling and simulation of an alkaline flow battery considering the tertiary current distribution on the electrodes: Anthraquinone-ferro/ferricyanide as organic electroactive species. *J. Power Sources* **2023**, *582*, 233533. [[CrossRef](#)]
31. Akuzum, B.; Alparslan, Y.C.; Robinson, N.C.; Agar, E.; Kumbur, E.C. Obstructed flow field designs for improved performance in vanadium redox flow batteries. *J. Appl. Electrochem.* **2019**, *49*, 551–561. [[CrossRef](#)]
32. Messaggi, M.; Gambaro, C.; Casalegno, A.; Zago, M. Development of innovative flow fields in a vanadium redox flow battery: Design of channel obstructions with the aid of 3D computational fluid dynamic model and experimental validation through locally-resolved polarization curves. *J. Power Sources* **2022**, *526*, 231155. [[CrossRef](#)]
33. Liu, Y.; Huang, Z.; Xie, X.; Liu, Y.; Wu, J.; Guo, Z.; Huang, Q. Redox flow battery: Flow field design based on bionic mechanism with different obstructions. *Chem. Eng. J.* **2024**, *498*, 155663. [[CrossRef](#)]
34. Gurieff, N.; Keogh, D.F.; Timchenko, V.; Menictas, C. Enhanced Reactant Distribution in Redox Flow Cells. *Molecules* **2019**, *24*, 3877. [[CrossRef](#)] [[PubMed](#)]
35. Gurieff, N.; Keogh, D.F.; Baldry, M.; Timchenko, V.; Green, D.; Koskinen, I.; Menictas, C. Mass Transport Optimization for Redox Flow Battery Design. *Appl. Sci.* **2020**, *10*, 2801. [[CrossRef](#)]
36. Dhillon, A. Multiphysics Modelling of an Alkaline All-Iron, All-Soluble Aqueous Redox Flow Battery. Master's Thesis, University of Waterloo, Waterloo, ON, Canada, 2021.
37. Chen, Z.; Yu, W.; Liu, Y.; Zeng, Y.; He, Q.; Tan, P.; Ni, M. Mathematical modeling and numerical analysis of alkaline zinc-iron flow batteries for energy storage applications. *Chem. Eng. J.* **2021**, *405*, 126684. [[CrossRef](#)]
38. Wang, Q.; Qu, Z.G.; Jiang, Z.Y.; Yang, W.W. Experimental study on the performance of a vanadium redox flow battery with non-uniformly compressed carbon felt electrode. *Appl. Energy* **2018**, *213*, 293–305. [[CrossRef](#)]
39. Knehr, K.W.; Agar, E.; Dennison, C.R.; Kalidindi, A.R.; Kumbur, E.C. A Transient Vanadium Flow Battery Model Incorporating Vanadium Crossover and Water Transport through the Membrane. *J. Electrochem. Soc.* **2012**, *159*, A1446. [[CrossRef](#)]
40. You, D.; Zhang, H.; Chen, J. A simple model for the vanadium redox battery. *Electrochim. Acta* **2009**, *54*, 6827–6836. [[CrossRef](#)]

**Disclaimer/Publisher's Note:** The statements, opinions and data contained in all publications are solely those of the individual author(s) and contributor(s) and not of MDPI and/or the editor(s). MDPI and/or the editor(s) disclaim responsibility for any injury to people or property resulting from any ideas, methods, instructions or products referred to in the content.